

Multidomain Galerkin-Collocation method: spherical collapse of scalar fields II

M. A. Alcoforado,^{1,*} R. F. Aranha,^{1,†} W. O. Barreto,^{1,2,‡} and H. P. de Oliveira^{1,§}

¹*Departamento de Física Teórica - Instituto de Física A. D. Tavares, Universidade do Estado do Rio de Janeiro, R. São Francisco Xavier, 524. Rio de Janeiro, RJ, 20550-013, Brazil*

²*Centro de Física Fundamental, Universidad de Los Andes, Mérida 5101, Venezuela*

(Dated: December 3, 2020)

We follow the strategy initiated in Ref. [1] and proceed with the implementation of the Galerkin-Collocation domain decomposition (GCDD) applied to the dynamics of a spherical self-gravitating scalar field with the field equation in the Cauchy formulation. We have adopted the areal slicing gauge. We have presented a detailed implementation for an arbitrary number of subdomains and adopted the simplest form of the transmission conditions. Further, by an appropriated choice of the basis functions in the inner subdomain, we eliminated exactly the $1/r$ terms near the origin present in the field equations. The code is validated using two error measures: the conservation of the ADM mass and the Hamiltonian constraint that must be satisfied during the spacetime dynamics. In general, both error measures converge exponentially in all subdomains. As a useful illustration of placing more subdomains near the strong-field region, meaning an efficient concentrating of collocation points near the origin, we exhibited the formation of an apparent horizon even though the numerical integration diverges.

I. INTRODUCTION

The present work is a continuation of the systematic development of the Galerkin-Collocation domains decomposition (GCDD) technique applied to problems of interest in numerical relativity. In Ref. [1], we have implemented an efficient algorithm to solve the field equations in the characteristic formulation describing the dynamics of a scalar field in spherically symmetric spacetimes, where we have included more than two subdomains. Here, our goal is to consider the same problem with the field equations in the Cauchy formulation. We have already implemented GCDD codes successfully in the following cases: (i) determination of the initial data for single [2] and binary black holes [3, 4], (ii) the dynamics of cylindrical gravitational waves [5], and (iii) critical collapse in the new characteristic scheme [6].

The domain decomposition or multidomain method consists of dividing the spatial domain into two or more subdomains and appropriate transmission conditions to connect the solutions in each subdomain. In the realm of spectral methods, the domain decomposition methods were first established for problems of fluid mechanics in the late 1970s. We indicate Canuto et al. [7] (see also Ref. [8]) for a helpful and concise presentation of domain decomposition methods. Orszag [9] introduced the spectral domain decomposition method for elliptic problems; Kopriva [10, 11] considered the spectral multidomain technique for hyperbolic problems. In this case, we remark that there is no unique way of matching the solutions in contiguous subdomains [10, 12].

The first application of the spectral domain decomposition method in Numerical Relativity was to determine the stationary configurations [13] and the initial data problem [14, 15]. For the time-dependent systems, the spectral domain decomposition was implemented within the SpEC [16] and LORENE [17] codes to deal with the gravitational collapse, the dynamics of stars and the evolution of single [18] and binary black holes [19]. A more detailed approach for the multidomain spectral codes is found in Refs. [20] and in the SXS collaboration [21].

The sequence of presentation is as follows. In the second Section, we establish the basic equations. We describe the domain-decomposition strategy in Section 3. As a typical feature of the adopted numerical strategy, we have introduced a compactified intermediary computational domain before separating it into several subdomains. We define the basis functions in each subdomain after establishing the corresponding rational Chebyshev polynomials. In Section 4, we proceed with the numerical tests to validate the multidomain code. We have considered two robust indicators from which we defined the error measures: the conservation of the ADM mass and the Hamiltonian constraint verification. As the last test, we have determined the formation of the apparent horizon and its mass, considering we have adopted a coordinate system that the integration diverges when the apparent horizon forms. In the last Section, we summarize the results and indicate the next steps of the present investigation line.

II. THE FIELD EQUATIONS

We present briefly the main equations and the basic aspects of the spherical collapse of a scalar field in the Cauchy scheme of the field equations. We adopt the fol-

* malcoforado@hotmail.com

† rafael.fernandes.aranha@uerj.br

‡ wobarreto@gmail.com

§ henrique.oliveira@uerj.br

lowing line element:

$$ds^2 = -e^{2\alpha} dt^2 + e^{2\mu} dr^2 + r^2(d\theta^2 \sin^2 \theta d\varphi^2), \quad (1)$$

with $\alpha = \alpha(t, r)$ and $\mu = \mu(t, r)$ determining the lapse function and the radial metric function, respectively. Considering a scalar field with potential $V(\phi)$, the relevant field equations are

$$\alpha_{,r} - \mu_{,r} + \frac{1}{r}(1 - e^{2\mu}) + re^{2\mu}V(\phi) = 0, \quad (2)$$

$$\mu_{,t} = \frac{r}{2} e^{\alpha-\mu} \Pi \phi_{,r}, \quad (3)$$

$$\mathcal{H} = \mu_{,r} + \frac{1}{2r}(e^{2\mu} - 1) - \frac{r}{4}(\Pi^2 + \phi_{,r}^2) - \frac{r}{2}e^{2\mu}V(\phi) = 0. \quad (4)$$

Eq. (2) is a consequence of the polar-areal slicing condition; Eqs. (3) and (4) are the momentum and the Hamiltonian constraints, respectively. We solve Eq. (2) to update the function $\alpha(t, r)$ in each time level or hypersurface slice, and we use Eq. (3) to evolve the metric function $\mu(t, r)$ instead of solving the Hamiltonian constraint at each slice (see, for instance [22–24]).

The Klein-Gordon equation

$$\square\phi = \frac{dV}{d\phi}, \quad (5)$$

can be split into two first-order equations:

$$\phi_{,t} = e^{\alpha-\mu} \Pi, \quad (6)$$

$$\Pi_{,t} = \frac{1}{r^2} (e^{\alpha-\mu} r^2 \phi_{,r})_{,r} - e^{\alpha+\mu} \frac{dV}{d\phi}, \quad (7)$$

with Eq. (6) defining the function $\Pi(t, r)$.

We integrate the field equations (2), (3), (6) and (7) starting with the initial data $\phi(t_0, r)$ and $\Pi(t_0, r)$. We determine the initial function $\mu(t_0, r)$ after solving the Hamiltonian constraint (4). Then, from Eq. (2) we obtain $\alpha(t_0, r)$, and from Eqs. (3), (6) and (7) we determine the initial functions $\mu_{,t}(t_0, r)$, $\phi_{,t}(t_0, r)$ and $\Pi_{,t}(t_0, r)$. With these quantities we fix the functions μ, ϕ, Π at the next time level, and the whole process repeats providing the evolution of the spacetime. We remark that we use the Hamiltonian constraint only to obtain the initial distribution $\mu(t_0, r)$. We further validate the code verifying the Hamiltonian constraint at each slice.

A relevant quantity is the mass function defined by:

$$1 - \frac{2m}{r} = g^{\mu\nu} r_{,\mu} r_{,\nu} = e^{-2\mu}, \quad (8)$$

that is, $m(t, r)$ measures the mass inside an sphere of radius r at the instant t . It can be shown that an apparent horizon forms when $\mu \rightarrow \infty$. Related to the mass function, we have the ADM mass

$$M_{ADM}(u) = \lim_{r \rightarrow \infty} m(t, r). \quad (9)$$

As mentioned, contrary to the Bondi mass, the ADM is conserved [25].

The boundary and coordinate conditions is an essential part to guarantee the regularity of the spacetime at the origin and the asymptotic flatness. Then, near the origin, we have

$$\alpha(t, r) = \mathcal{O}(r^2), \quad (10)$$

$$\mu(t, r) = \mathcal{O}(r^2), \quad (11)$$

$$\phi(t, r) = \phi_0(t) + \mathcal{O}(r^2), \quad (12)$$

$$\Pi(t, r) = \Pi_0(t) + \mathcal{O}(r^2). \quad (13)$$

We pointed out that the cancellation of the $1/r$ terms present in the field equations requires fulfilling the above conditions. As we are going to show, with the Galerkin-Collocation method, these conditions are satisfied exactly.

The asymptotic conditions are

$$\alpha(t, r) = \alpha_0(t) + \frac{\alpha_{-1}(t)}{r} + \mathcal{O}(r^{-2}), \quad (14)$$

$$\mu(t, r) = \frac{M_{ADM}}{r} + \mathcal{O}(r^{-2}), \quad (15)$$

$$\phi(t, r) = \hat{\phi}_0 + \frac{\hat{\phi}_{-1}(t)}{r} + \mathcal{O}(r^{-2}), \quad (16)$$

$$\Pi(t, r) = \frac{\Pi_{-2}(t)}{r^2} + \mathcal{O}(r^{-3}). \quad (17)$$

We remark that for a massless scalar field, we set $\hat{\phi}_0 = 0$, but depending on the potential we may have $\hat{\phi}_0 \neq 0$ and/or $\hat{\phi}_{-1} = 0$. Also, from the asymptotic expansion of the function $\mu(t, r)$, we can read off the ADM mass.

The mass function satisfies the equation

$$\frac{\partial m}{\partial r} = \frac{r^2}{4} e^{-2\mu} (\Pi^2 + \phi_{,r}^2) + \frac{r^2}{2} V(\phi), \quad (18)$$

that is obtained after deriving Eq. (8) and taking into account the Hamiltonian constraint (4). We calculate the ADM mass integrating the above expression yielding

$$M_{ADM} = \int_0^\infty \left[\frac{r^2}{4} e^{-2\mu} (\Pi^2 + \phi_{,r}^2) + \frac{r^2}{2} V(\phi) \right] dr. \quad (19)$$

We point out that the ADM mass calculation is performed more accurately using the above integral expression.

III. THE MULTIDMOAIN GALERKIN-COLLOCATION METHOD

We describe the numerical procedure based on the Galerkin-Collocation method in multiple nonoverlapping

subdomains applied to a self-gravitating scalar field described by Eqs. (2), (3), (6) and (7). We follow the same line of the presentation we have done in Ref. [1] for the case of the characteristic scheme.

- Spectral approximations

We divided the physical domain $\mathcal{D} : 0 \leq r < \infty$ into several subdomains $\mathcal{D}_1 : 0 \leq r \leq r_{(1)}, \dots, \mathcal{D}_l : r_{(l-1)} \leq r \leq r_{(l)}, \dots, \mathcal{D}_n : r_{(n-1)} \leq r < \infty$, with $r_0 = 0$, and $r_{(1)}, r_{(2)}, \dots, r_{(n-1)}$ representing the interface between contiguous subdomains.

In each subdomain, we establish the spectral approximations of the metric functions $\alpha(t, r)$, $\mu(t, r)$ and the scalar field functions $\phi(r, t)$, $\Pi(t, r)$:

$$\alpha^{(l)}(t, r) = \sum_{k=0}^{N_\alpha^{(l)}} \hat{\alpha}_k^{(l)}(t) \Phi_k^{(l)}(r), \quad (20)$$

$$\mu^{(l)}(t, r) = \sum_{k=0}^{N_\mu^{(l)}} \hat{\mu}_k^{(l)}(t) \Xi_k^{(l)}(r), \quad (21)$$

$$\phi^{(l)}(t, r) = \sum_{k=0}^{N_\phi^{(l)}} \hat{\phi}_k^{(l)}(t) \psi_k^{(l)}(r), \quad (22)$$

$$\Pi^{(l)}(t, r) = \sum_{k=0}^{N_\Pi^{(l)}} \hat{\Pi}_k^{(l)}(t) \chi_k^{(l)}(r), \quad (23)$$

where $l = 1, 2, \dots, n$ indicates the specific subdomain; $\{\hat{\alpha}_k^{(l)}(t), \hat{\mu}_k^{(l)}(t), \hat{\phi}_k^{(l)}(t), \hat{\Pi}_k^{(l)}(t)\}$ are the modes or the unknown coefficients and $\{\Phi_k^{(l)}(r), \Xi_k^{(l)}(r), \psi_k^{(l)}(r), \chi_k^{(l)}(r)\}$ are basis functions. We fix the number of modes in each subdomain by the truncation orders $N_\alpha^{(l)}, N_\mu^{(l)}, N_\phi^{(l)}, N_\Pi^{(l)}$, $l = 1, 2, \dots, n - 1$. According with the Galerkin method, the basis functions belonging to the first and last subdomains must satisfy the boundary conditions (10) - (13) and (14) - (17), respectively. The basis functions in the intermediate subdomains $l = 2, 3, \dots, n - 1$ are identified as the rational Chebyshev polynomials [26] defined in these subdomain as we are going to define in the sequence.

- Rational Chebyshev polynomials

We define the rational Chebyshev polynomials in each subdomain using Fig. 1 to indicate the mappings we have adopted to connect the physical and the computational subdomains. First, the domain $\mathcal{D}_l : 0 \leq r < \infty$ is mapped into the interval $-1 \leq x \leq 1$ using the algebraic map [26]

$$r = L_0 \frac{(1+x)}{1-x}, \quad (24)$$

where L_0 is the map parameter and $x^{(1)}, x^{(2)}, \dots, x^{(n-1)}$ are the interface between contiguous subdomains as shown in Fig. 1. Second, we introduce linear transfor-

mations to define the computational subdomains parameterized by $-1 \leq \xi^{(l)} \leq 1$, $l = 1, 2, \dots, n$:

$$x(\xi^{(l)}) = \frac{1}{2} \left[\left(x^{(l)} - x^{(l-1)} \right) \xi^{(l)} + x^{(l)} + x^{(l-1)} \right], \quad (25)$$

with $l = 0, 1, \dots, n$ where $x^{(0)} = -1$ and $x^{(n)} = 1$. These computational subdomains are the loci of the collocation points that are mapped back to r_k in the physical domain \mathcal{D} .

The rational Chebyshev polynomials are defined in each subdomains as

$$TL_k^{(l)} = T_k \left(\xi^{(l)} = \frac{a^{(l)}r + b^{(l)}}{(r + L_0)} \right), \quad (26)$$

where

$$a^{(l)} = \frac{2L_0 + r^{(l)} + r^{(l-1)}}{r^{(l)} - r^{(l-1)}}, \quad (27)$$

$$b^{(l)} = -\frac{2r^{(l)}r^{(l-1)} + L_0(r^{(l)} + r^{(l-1)})}{r^{(l)} - r^{(l-1)}}. \quad (28)$$

$T_k(\xi)$ is the Chebyshev polynomial of k th order, $r^{(l-1)} \leq r \leq r^{(l)}$ corresponds to $-1 \leq \xi^{(l)} \leq 1$ for all $l = 1, 2, \dots, n$ with $r^{(0)} = 0$ and $r^{(n)}$ is located at the infinity.

- Basis functions

We can now define the basis functions for the spectral approximations (20) - (23). The rational Chebyshev polynomials (26) are the basis functions for all spectral approximations in the subdomains $\mathcal{D}_l, l = 2, 3, \dots, n - 1$. For the subdomains \mathcal{D}_1 and \mathcal{D}_n the basis functions must satisfy the conditions (10) - (13) and (14) - (17), respectively.

The basis for the functions $\alpha(t, r)$ and $\mu(t, r)$ in the first subdomain \mathcal{D}_1 are

$$\begin{aligned} \Phi_k^{(1)}(r) = \Xi_k^{(1)}(r) &= \frac{(1+2k)}{4(3+2k)} TL_{k+2}^{(1)}(r) \\ &+ \frac{(1+k)}{3+2k} TL_{k+1}^{(1)}(r) + \frac{1}{4} TL_k^{(1)}(r). \end{aligned} \quad (29)$$

As a consequence, we have $\Phi_k^{(1)}(r) = \mathcal{O}(r^2)$. Concerning the scalar field basis functions, we have adopted a distinct approach by using the Tau method [26]. To reproduce the conditions (16) and (17), we assume that $\psi_k^{(1)}(r) = \chi_k^{(1)}(r) = TL_k^{(1)}(r)$ and impose a relation between the modes $\hat{\phi}_k^{(1)}(t)$ such that

$$\left(\frac{\partial \phi^{(1)}}{\partial r} \right)_{r=0} = \sum_{k=0}^{N_\phi^{(1)}} \hat{\phi}_k^{(1)}(t) \left(\frac{dTL_k^{(1)}}{dr} \right)_{r=0} = 0. \quad (30)$$

A similar relation is established for the function $\Pi^{(1)}(t, r)$.

In the subdomain \mathcal{D}_n , the basis for the function $\alpha^{(n)}(t, r)$ is simply the rational Chebyshev polynomial, or $\Phi_k^{(n)} = TL_k^{(n)}(r)$. Since the asymptotic behaviors of

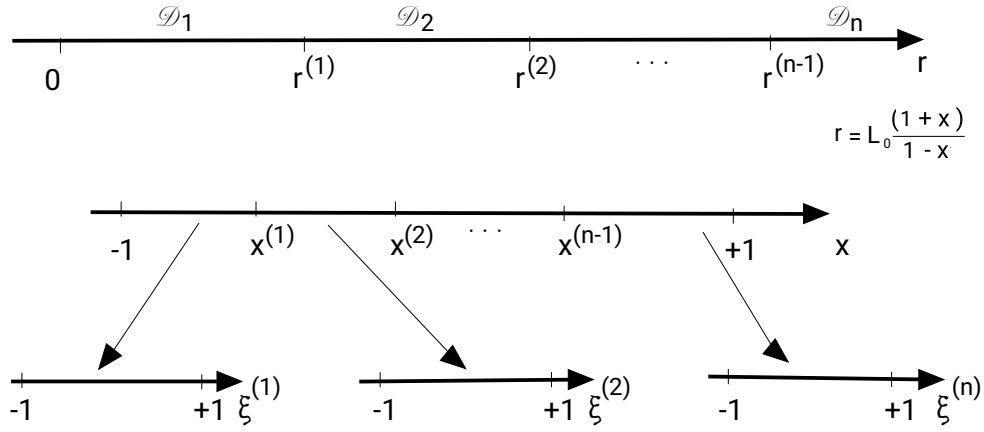


FIG. 1. Basic scheme showing the subdomains $\mathcal{D}_1, \mathcal{D}_2, \dots, \mathcal{D}_n$ covered by $-1 \leq \xi^{(j)} \leq 1$, $k = 1, 2, \dots, n$, and the intermediate computational subdomain $-1 \leq x \leq 1$.

Table 1

	\mathcal{D}_1	\mathcal{D}_2	...	\mathcal{D}_{n-1}	\mathcal{D}_n
α	$\Phi_k^{(1)}(r)$	$TL_k^{(l)}(r)$			$TL_k^{(n)}(r)$
μ	$\Phi_k^{(1)}(r)$				$\psi_k^{(n)}(r)$
ϕ	$TL_k^{(1)}(r)^{(*)}$				$\psi_k^{(n)}(r)$
Π	$TL_k^{(1)}(r)^{(*)}$				$\chi_k^{(n)}(r)$

TABLE I. Basis functions for the spectral approximations (20) - (23). The asterisks indicate restriction imposed to the modes $\hat{\phi}_k^{(1)}$ and $\hat{\Pi}_k^{(1)}$ to satisfy the conditions (16) and (17).

the functions $\mu^{(n)}(t, r)$ and $\phi^{(n)}(t, r)$ are identical with the caveat $\hat{\phi}_0 = 0$, we have

$$\Xi_k^{(n)}(r) = \psi_k^{(n)}(r) = \frac{1}{2}(TL_{k+1}^{(n)}(r) - TL_k^{(n)}(r)). \quad (31)$$

To reproduce the asymptotic behavior (17), the basis for the function $\Pi^{(n)}(t, r)$ is expressed by a linear combination of the rational Chebyshev polynomials given by

$$\chi_k^{(n)}(r) = -\frac{(1+2k)}{4(3+2k)}TL_{k+2}^{(n)}(r) + \frac{(1+k)}{3+2k}TL_{k+1}^{(n)}(r) - \frac{1}{4}TL_k^{(n)}(r). \quad (32)$$

For the sake of completeness, we summarize the presentation of the basis functions in Table 1.

- Transmission conditions

The next step is to establish the transmission conditions to guarantee that all pieces of the spectral approximations (20) - (23) represent the same functions but defined in each subdomain. We adopt the patching method [7] that demands that a function and all their $d-1$ spatial derivatives must be continuous at the contiguous subdomains' interface. However, in the present case we introduce a slight modification consisting of imposing that all

functions and their first derivatives with r are continuous at the interfaces. Then, we have the following transmission conditions:

$$\alpha^{(l)}(t, r^{(l)}) = \alpha^{(l+1)}(t, r^{(l)}), \quad (33)$$

$$\left(\frac{\partial \alpha}{\partial r}\right)_{r^{(l)}}^{(l)} = \left(\frac{\partial \alpha}{\partial r}\right)_{r^{(l)}}^{(l+1)}, \quad (34)$$

$$\mu^{(l)}(t, r^{(l)}) = \mu^{(l+1)}(t, r^{(l)}), \quad (35)$$

$$\left(\frac{\partial \mu}{\partial r}\right)_{r^{(l)}}^{(l)} = \left(\frac{\partial \mu}{\partial r}\right)_{r^{(l)}}^{(l+1)}, \quad (36)$$

$$\phi^{(l)}(t, r^{(l)}) = \phi^{(l+1)}(t, r^{(l)}), \quad (37)$$

$$\left(\frac{\partial \phi}{\partial r}\right)_{r^{(l)}}^{(l)} = \left(\frac{\partial \phi}{\partial r}\right)_{r^{(l)}}^{(l+1)}, \quad (38)$$

with $l = 1, 2, \dots, n$, and the same conditions for the function $\Pi(t, r)$. We remark that the number of transmission conditions restricts the number of collocation or grid points in the subdomains.

- Implementing the GC domain decomposition method

The goal of any spectral method is to approximate a set of evolution partial differential equations into a finite set of ordinary differential equations. By considering the system formed by the equations (2), (3), (6) and (7), we approximate them by sets of dynamical systems for the modes $\hat{\phi}_k^{(l)}(t)$, $\hat{\Pi}_k^{(l)}(t)$ and $\hat{\mu}_k^{(l)}(t)$ with $l = 1, 2, \dots, n$. In this direction, the field equation (2) results in a set of algebraic equations for the modes $\hat{\alpha}_k^{(l)}(t)$. The description of the procedure follows closely our previous reference [1], and also is a generalization of the procedure outlined in Refs. [5, 6].

We indicate briefly derivation of the dynamical systems and the algebraic set of equations above mentioned.

More details can be found in Refs. [1, 5, 6]. By substituting the spectral approximations (20) - (23) into the field equations (2), (3), (6) and (7) we obtain the corresponding residual equations. For instance, taking Eq. (3), the residual equations in each subdomain become

$$\text{Res}_\mu^{(l)}(t, r) = \sum_{k=0}^{N_\mu^{(l)}} \hat{\mu}_{k,t}^{(l)} \Xi_k^{(l)}(r) - \frac{r}{2} (e^{\alpha-\mu} \Pi \phi, r)^{(l)}, \quad (39)$$

$l = 1, 2, \dots, n$. These equations do not vanish due to the approximations established for the metric and scalar field functions. We follow the prescription of the Collocation method to determine the dynamical system for the modes $\bar{\mu}_k^{(l)}(u)$, meaning to vanish the residual equations (39) at the corresponding collocation points located in each subdomain. Then

$$\text{Res}_\mu^{(l)}(t, r_j^{(l)}) = 0. \quad (40)$$

where $r_j^{(l)}$ are the collocation points in the physical domain related to the collocation points $-1 \leq \xi_j^{(l)} \leq 1$ in the computational subdomains by

$$r_j^{(l)} = \frac{b^{(l)} - L_0 \xi_j^{(l)}}{\xi_j^{(l)} - a^{(l)}}, \quad (41)$$

with $a^{(l)}, b^{(l)}$ given by the relations (27) and (28), respectively. The total amount of the collocation points, $\xi_j^{(l)}$ in the computational subdomains must be

$$\underbrace{\sum_{l=1}^n N_\mu^{(l)} + n}_{\text{number of modes } \hat{\mu}_k^{(l)}} - \underbrace{2(n-1)}_{\text{transmission conditions}} = \underbrace{\sum_{l=1}^n N_\mu^{(l)} - n + 2}_{\text{number of collocation points}},$$

where $n \geq 2$. Therefore, we have $\sum_{l=1}^n N_\mu^{(l)} - n + 2$ equations (40). These equations together with the transmission conditions (35) and (36) allow to determine the dynamical system for the modes $\hat{\mu}_k^{(l)}$ written schematically as

$$\frac{d\hat{\mu}_k^{(l)}}{dt} = F_k^{(l)}(\alpha, \mu, \Pi, \phi, r), \quad (42)$$

where $k = 0, 1, \dots, N_\mu^{(l)}$ and $l = 1, 2, \dots, n$ and the arguments on the RHS represent the values of these functions at the collocation points belonging to all subdomains.

We choose $\xi_j^{(l)}$ as the Chebyshev-Gauss-Lobatto points [27] in each subdomain:

$$\xi_j^{(1)} = \cos\left(\frac{j\pi}{N_\mu^{(1)} + 1}\right), \quad j = 1, 2, \dots, N_\mu^{(1)}, \quad (43)$$

$$\xi_j^{(l)} = \cos\left(\frac{j\pi}{N_\mu^{(l)} - 1}\right), \quad j = 1, 2, \dots, N_\mu^{(l)} - 1, \quad (44)$$

Table 2

	\mathcal{D}_1	\mathcal{D}_2	...	\mathcal{D}_{n-1}	\mathcal{D}_n
α	$N_\alpha^{(1)}$	$N_\alpha^{(2)} - 1$...	$N_\alpha^{(n-1)} - 1$	$N_\alpha^{(n)}$
μ	$N_\mu^{(1)}$	$N_\mu^{(2)} - 1$...	$N_\mu^{(n-1)} - 1$	$N_\mu^{(n)}$
ϕ	$N_\phi^{(1)}$	$N_\phi^{(2)} - 1$...	$N_\phi^{(n-1)} - 1$	$N_\phi^{(n)}$
Π	$N_\Pi^{(1)}$	$N_\Pi^{(2)} - 1$...	$N_\Pi^{(n-1)} - 1$	$N_\Pi^{(n)}$

TABLE II. Distribution of the collocation points in each subdomains according to corresponding truncation orders.

for $l = 2, \dots, n - 1$, and for the last subdomain

$$\xi_j^{(n)} = \cos\left(\frac{j\pi}{N_\mu^{(n)}}\right), \quad j = 1, 2, \dots, N_\mu^{(n)}. \quad (45)$$

The number of collocation points in each subdomain follows the distribution depicted in Table 2. As in Ref. [1], we have placed the interfaces $r^{(1)}, r^{(2)}, \dots, r^{(n-1)}$ as belonging to the corresponding subsequent subdomains, $\mathcal{D}_2, \mathcal{D}_3, \dots, \mathcal{D}_n$, respectively.

The origin is not a collocation point of (43) since the equation for the metric function $\mu(t, r)$ is satisfied automatically due to the choice of the basis function in the first subdomain, $\Xi_k^{(1)}(r) = \Phi_k^{(1)}(r)$ (cf. Table 1). Furthermore, the same feature is valid for Eq. (2) for the function $\alpha(t, r)$. For this reason, the same structure of collocation points (43) - (45) will be used for projecting the residual equation associated to Eq. (2). Repeating the same steps as outlined previously, we obtain

$$\hat{\alpha}_k^{(l)} = G_k^{(l)}(\mu, \mu, r, \phi), \quad (46)$$

where $k = 0, 1, \dots, N_\alpha^{(l)}$ and $l = 1, \dots, n$. Again, the arguments on the RHS of the above equation represent the values of μ, μ, r and ϕ at the collocation points of all subdomains.

The final step is to obtain the dynamical systems that approximate the evolution equations (6) and (7). After establishing the corresponding residual equations and choosing the collocation points in each subdomain, the sets of equations for $\hat{\phi}_k^{(l)}$ and $\hat{\Pi}_k^{(l)}$ are

$$\frac{d\hat{\phi}_k^{(l)}}{dt} = H_k^{(l)}(\alpha, \mu, \phi, r), \quad k = 0, 1, \dots, N_\phi^{(l)} \quad (47)$$

$$\frac{d\hat{\Pi}_k^{(l)}}{dt} = J_k^{(l)}(\alpha, \alpha, r, \mu, \mu, r, \phi, \phi, r, \phi, r, r), \quad (48)$$

$$k = 0, 1, \dots, N_\Pi^{(l)},$$

and $l = 1, 2, \dots, n$. Again, the RHS depends on the values of the arguments at the collocation points in all subdomains.

The number of collocation points in the subdomains to

generate, for instance, the system (47), is

$$\underbrace{\sum_{l=1}^n N_\phi^{(l)}}_{\text{number of modes } \hat{\phi}_k^{(l)}} + n - \underbrace{2(n-1)}_{\text{transmission conditions}} = \underbrace{\sum_{l=1}^n N_\phi^{(l)} - n + 2}_{\text{number of collocation points}},$$

By substituting $N_\phi^{(l)}$ by $N_\Pi^{(l)}$, we have the number of collocation points for the modes $\hat{\Pi}^{(l)}$. We have chosen the Chebychev-Gauss-Lobatto points and presented their distribution in each subdomain in Table 2. In this case, for the first, $l = 1$ and the last, $l = n$ subdomains, we have $N_\phi^{(1)}$ ($N_\Pi^{(1)}$) collocation points:

$$\xi_j^{(l)} = \cos\left(\frac{j\pi}{N_\phi^{(l)}}\right), \quad \text{if } l = 1, n, \quad (49)$$

where $j = 0, 1, \dots, N_\phi^{(1)}$ and $j = 1, 2, \dots, N_\phi^{(n)}$, for the first and the last subdomains, respectively. And for all other subdomains, it follows

$$\xi_j^{(l)} = \cos\left(\frac{j\pi}{N_\phi^{(l)} - 1}\right), \quad \text{if } l = 2, \dots, n-1, \quad (50)$$

where $j = 1, 2, \dots, N_\phi^{(l)} - 1$. The same distribution and structure of the collocation points is valid for the residual equation of $\Pi(t, r)$ after substituting above $N_\phi^{(l)}$ by $N_\Pi^{(l)}$.

We would like to make some pertinent and brief comments. The sets of collocation points (43) - (45) and (49) - (50) have identical structure; the exception is that the origin is included in the second set. We have placed the interfaces $r^{(1)}, r^{(2)}, \dots, r^{(n-1)}$ as belonging to the corresponding subsequent subdomains, $\mathcal{D}_2, \mathcal{D}_3, \dots, \mathcal{D}_n$, respectively, as implemented in Ref. [1].

In closing this Section, we point out that the domain decomposition method applied to hyperbolic problems does not fix the transmission conditions [10, 11]. The delicate problem is to choose the proper way the information is transmitted through several subdomains, which is crucial to provide a stable code. In establishing the transmission conditions (35) - (36) for the dynamical functions, we have adopted their simplest form and enforcing that each interface constitutes a collocation point of the subsequent subdomain. As we will show in the next Section, the code is stable and converge exponentially no matter the chosen error measure.

IV. CODE VALIDATION: NUMERICAL RESULTS

We present the numerical tests to validate the domain decomposition GC algorithm by investigating the influence of increasing the resolution in each subdomain and the number of subdomains. In all numerical experiments, we integrate the dynamical systems (42), (47), and (48)

with a fourth-order Runge-Kutta integrator. Furthermore, we have adopted a strategy of dividing the intermediate computational domain covered by $-1 \leq x \leq 1$ (cf. Fig. 1) in equal parts. It means that in the case of two subdomains, for instance, $x^{(1)} = 0$ implying in $r^{(1)} = L_0$; for three subdomains, we have $x^{(1)} = -1/3$ and $x^{(2)} = 1/3$ yielding $r^{(1)} = L_0/2$ and $r^{(2)} = 2L_0$, respectively, and so on. Consequently, the information about the location of the interfaces is determined by the map parameter L_0 . Unless stated otherwise, we adopt the following, say ‘‘economic’’ rule for choosing the truncation orders that appear in the spectral approximation (20) - (23). First, we fix $N_\phi^{(1)}$ then $N_\phi^{(2)} = N_\phi^{(1)} + 1$, and $N_\phi^{(3)} = 1.1N_\phi^{(1)}$; the truncation orders for the function $\Pi(t, r)$ satisfy the same rule. On the other side, we have $N_\alpha^{(1)} = N_\phi^{(1)}$, $N_\alpha^{(2)} = N_\phi^{(2)}$, $N_\alpha^{(3)} = 1.2N_\phi^{(1)}$, and the same truncation orders for the function $\mu(t, r)$. Notice that in each subdomain, we have two sets of collocation points; one for the functions $\phi(t, r)$ and $\Pi(t, r)$, and another for the metric functions $\alpha(t, r)$ and $\mu(t, r)$.

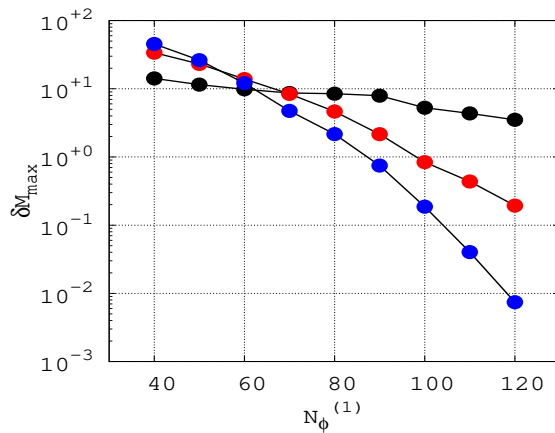


FIG. 2. Exponential decay of δM for $L_0 = 1.0$ (black circles), 3.0 (red circles) and 5.0 (blue circles) for a code with two subdomains. $N_\phi^{(1)}$ is the truncation order in the first domain taken as a reference.

The numerical experiments to validate the present algorithm start with the initial data taken from the Alcubierre’s book [29]

$$\phi_0(r) = A_0 r^2 e^{-(r-r_0)^2/\sigma^2}, \quad (51)$$

where $\sigma = 1.0$, $r_0 = 5.0$ and A_0 is the initial amplitude left as a free parameter. We also assume that $\Pi(0, r) = \Pi_0(r) = 0$, and the initial function $\mu(0, r) = \mu_0(r)$ is determined after solving the Hamiltonian constraint (4).

The first numerical test consists of verifying the conservation of the ADM mass. We calculate the relative deviation, δM , according to

$$\delta M = \frac{|M_{ADM}(0) - M_{ADM}(t)|}{M_{ADM}(0)} \times 100, \quad (52)$$

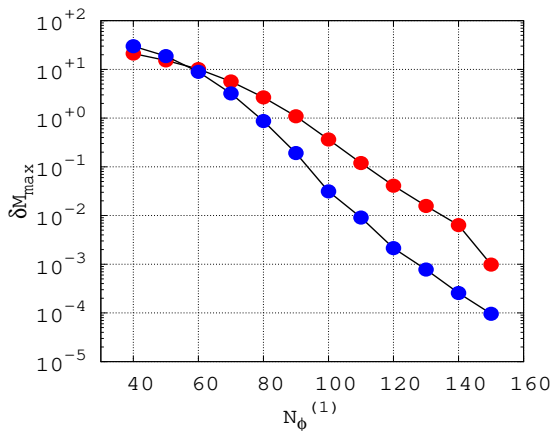


FIG. 3. Exponential decay of the maximum relative deviation δM_{\max} for $L_0 = 2.0$ (red circles), and 3.0 (blue circles) produced by a code with three subdomains. $N_\phi^{(1)}$ is the truncation order in the first domain taken as a reference.

where $M_{ADM}(0)$ is the initial ADM mass and $M_{ADM}(t)$ is its corresponding numerical value at an instant t . In all simulations, we choose the initial scalar field amplitude $A_0 = 0.008$ that is close to the formation of an apparent horizon ($A_0 \gtrsim 0.0082$), therefore providing a typical nonlinear evolution.

We calculate the ADM using the integral formula (4) taking advantage of the scheme shown in Fig. 1 by splitting the integral to a sum of integrals evaluated in the corresponding computational subdomains covered by $-1 \leq \xi^{(l)} \leq 1$, $l = 1, 2, \dots, n$, or

$$M_{ADM} = \sum_{l=1}^n \int_{-1}^1 \left[\frac{r^2}{4} e^{-2\mu} (\Pi^2 + \phi_{,r}^2) \right]^{(l)} \left(\frac{dr}{d\xi} \right)^{(l)} d\xi^{(l)}, \quad (53)$$

where n is the number of subdomains, the factor $dr/d\xi$ is calculated using the relation (41), and we have considered a massless scalar field. We further approximate each integral with quadrature formulae [28] as

$$\int_{-1}^1 \left[\frac{r^2}{4} e^{-2\mu} (\Pi^2 + \phi_{,r}^2) \right]^{(l)} \left(\frac{dr}{d\xi} \right)^{(l)} d\xi^{(l)} \approx \sum_{k=0}^{N_q} (\dots)_k^{(l)} w_k^{(l)}. \quad (54)$$

In the above expression, $w_k^{(l)}$ represents the weights, $N_q = 1.5N_\phi^{(l)}$ is the quadrature truncation order defined in each subdomain, and $(\dots)_k$ denote the values of the integrand at the quadrature collocation points assumed to be the Lagrange-Gauss-Lobatto points [28]. Also, in evaluating the integrals, we have used the spectral approximations (20) - (23).

With a code with two subdomains, we present in Fig. 2 the decay of the maximum value of δM with the increase

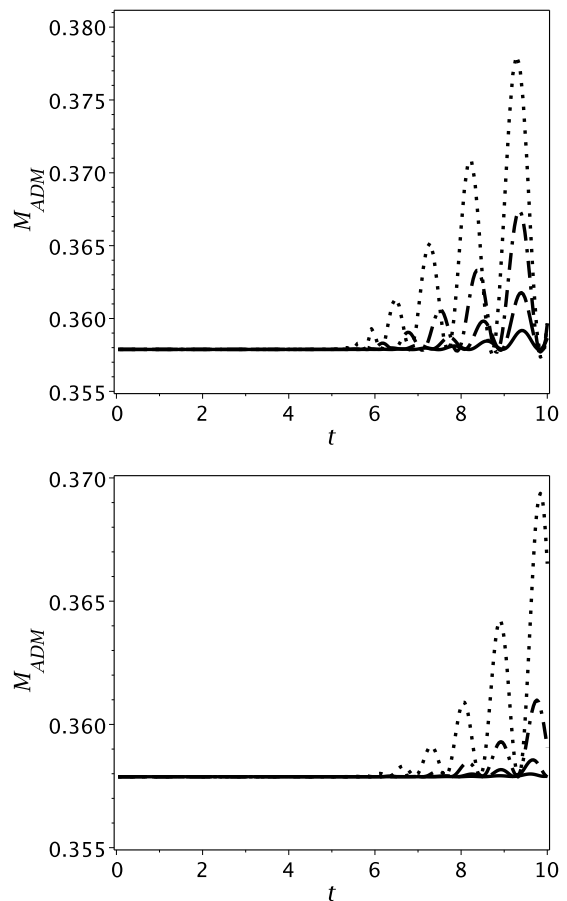


FIG. 4. Illustration of the conservation of the ADM mass produced by the code with three subdomains: $L_0 = 2.0$ (upper panel) and 3.0 (lower panel).

of the resolution represented by the first subdomain's truncation, $N_\phi^{(l)}$ order as a reference. We have tested three values of the map parameter, $L_0 = 1.0, 3.0$, and 5.0 (boxes, diamonds, and circles, respectively), fixing the interfaces between the subdomains at $r^{(1)} = 1.0, 3.0$ and 5.0 respectively. The maximum deviation, δM_{\max} , decays exponentially at distinct rates depending on L_0 . From these results, the large is L_0 , more rapidly δM_{\max} decays. By increasing the map parameter, the size of the second subdomain decreases, improving its numerical resolution and explaining the results of Fig. 2.

We repeat the same numerical test in Fig. 3 with three subdomains taken two values of the map parameter, $L_0 = 2.0$ and 3.0 , which places the subdomains interfaces at $r^{(1)} = 0.5$, $r^{(2)} = 2$, and $r^{(1)} = 1.5$, $r^{(2)} = 6$, respectively. As expected, better convergence is achieved for $L_0 = 3.0$, where the minimum deviation in the value of the ADM mass is about one part in 10^5 . To illustrate the effect of increasing the truncation order in the conservation of the ADM mass, we present in Fig. 4(a) and 4(b) several ADM plots for $L_0 = 2.0$ and 3.0 with $N_\phi^{(1)} = 70, 80, \dots, 100$, respectively. For $L_0 = 3.0$ and

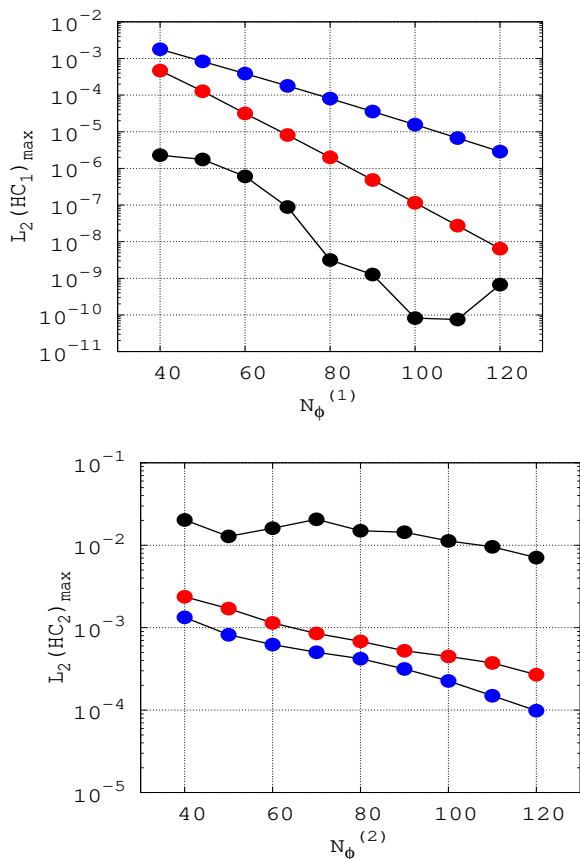


FIG. 5. Decay of the maximum L_2 -error associated to the Hamiltonian constraint in the first (upper panel) and second (lower plot) subdomains. We have used three values of the map parameter: $L_0 = 1.0$ (black circles), $L_0 = 3.0$ (red circles) and $L_0 = 5.0$ (blue circles). $N_\phi^{(1)}$ and $N_\phi^{(2)}$ are the truncation orders of the scalar field in the first and second subdomains, respectively.

$N_\phi^{(1)} = 100$, the maximum deviation is about $10^{-3}\%$ producing an almost constant plot of the ADM mass.

The next numerical test is the validity and convergence of the Hamiltonian constraint (4). We proceed by calculating the L_2 -error associated with the Hamiltonian constraint at each subdomain. Then, we may write

$$L_2(HC^{(l)}) = \sqrt{\frac{1}{2} \int_{-1}^1 (\mathcal{H}^{(l)})^2 d\xi^{(l)}}, \quad (55)$$

with $l = 1, 2, \dots, n$, and the integral is calculated using a quadrature formula.

We calculate the above L_2 -error with two and three subdomains using the same truncation orders of Fig. 2 and 3. In Fig. 5, we show the exponential decay of the maximum error in the first and second subdomains for $L_0 = 1.0$ (black circles), 2.0 (red circles), and 5.0 (blue circles). The effect of increasing the map parameter produces an increase of the maximum error in the first subdomain ($\mathcal{D}_1 : 0 \leq r \leq L_0$). Notice that if we fix

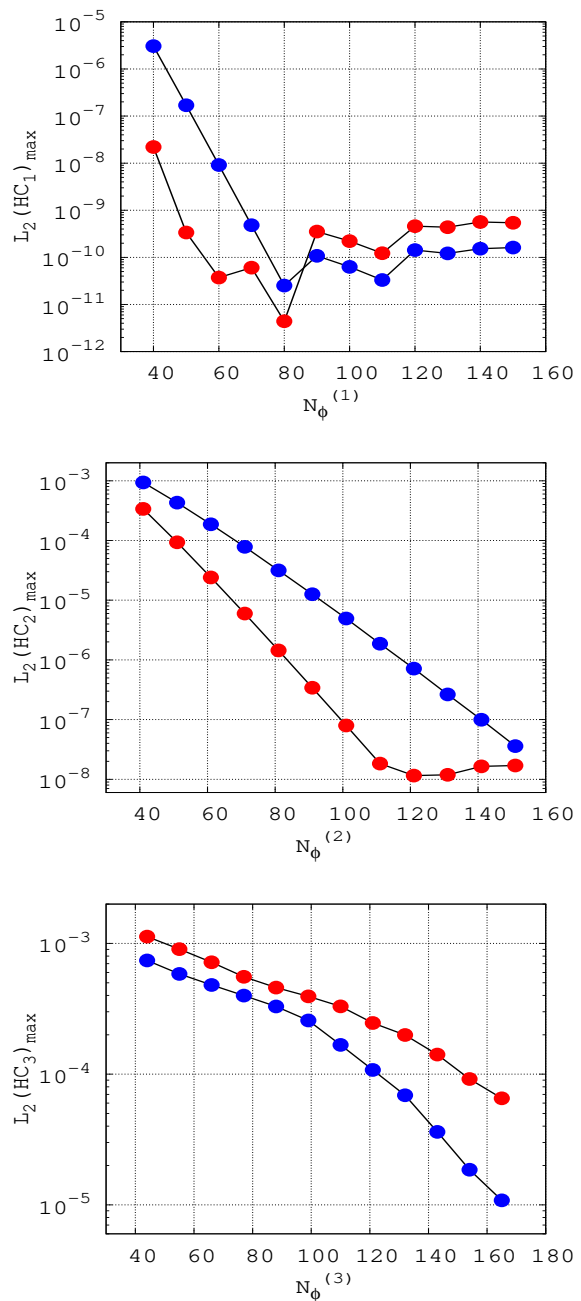


FIG. 6. Decay of the maximum L_2 -error associated to the Hamiltonian constraint in the first, second and third subdomains, from up to down. We have used two values of the map parameter, $L_0 = 2.0$ (red) and 3.0 (blue). $N_\phi^{(1)}$, $N_\phi^{(2)}$ and $N_\phi^{(3)}$ are the truncation orders of the scalar field in the first, second and third subdomains, respectively.

the truncation order, the subdomain's increase means a smaller numerical resolution and more significant errors. For instance, for $N_\phi^{(1)} = 120$, we obtain $L_2(HC^{(1)})_{\max} \sim \mathcal{O}(10^{-9})$, $\mathcal{O}(10^{-8})$, $\mathcal{O}(10^{-6})$ for $L_0 = 1.0, 3.0$, and 5.0 , respectively. These results are very satisfactory, but the most important feature is the exponential decay of the

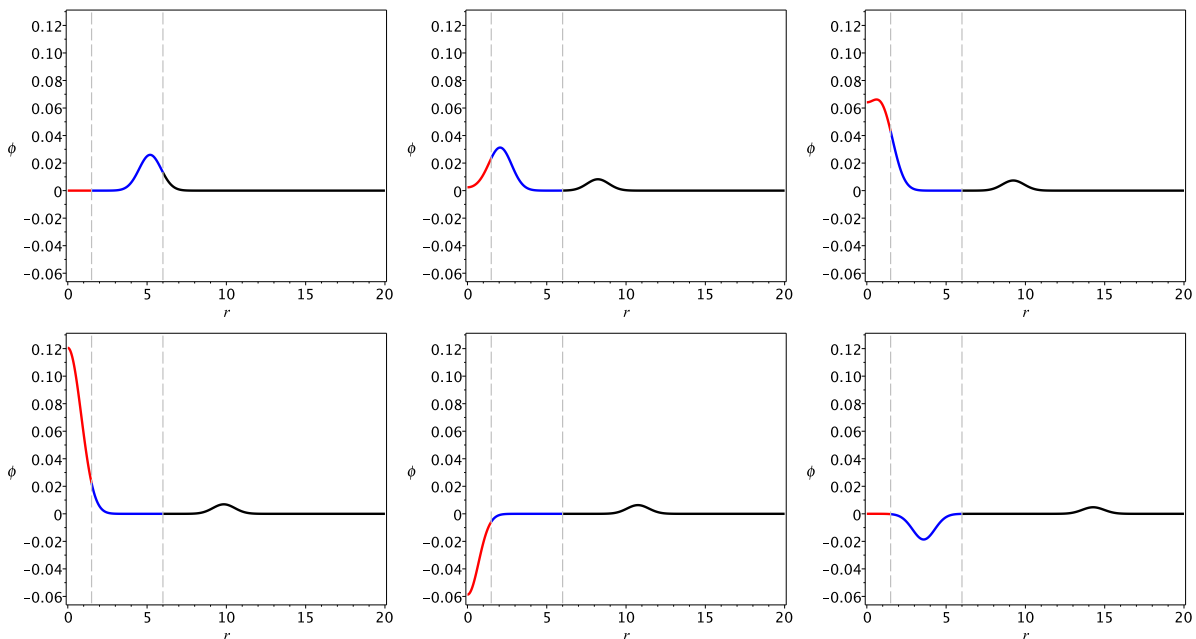


FIG. 7. Snapshots of the scalar field calculated at $t = 0, 3, 4, 4.6, 5.5$ and 10 from top to bottom, left to right. Here, the initial amplitude is $A_0 = 0.002$ and the pulse is centered initially at $r_0 = 5$ (cf. Eq. (51)).

maximum error that guarantees a fast code convergence. On the other hand, the opposite occurs for the second subdomain; that is, the increase of L_0 improves the error decay considerably, as shown in the lower panel of Fig. 5(b).

Next, we reproduce the snapshots of the scalar field's evolution, starting with the amplitude $A_0 = 0.001$, the same adopted in Ref. [29]. As stated in this reference, this amplitude is large but not enough to form an apparent horizon. We have considered the evolution produced by a three subdomain code with $N_\phi^{(1)} = 80$, $N_\phi^{(2)} = 81$, and $N_\phi^{(3)} = 88$ with the snapshots displayed in Fig. 7 corresponding to the instants $t = 0, 1, 3, 4, 4.6, 5.5, 10$. In the panels, we included the location of the subdomains with the red, blue, and black lines correspond to the first, second, and third subdomains, respectively.

The scalar field pulse separates into two parts traveling in opposite directions. The ingoing pulse implodes at the origin, reaching to a maximum amplitude of 0.12 while the outgoing component is located at $r \approx 10$ in agreement with the simulation of Ref. [29]. However, it occurs at $t \approx 4.6$ instead of $t = 5.0$. The discrepancy is due to the use of a different gauge for the lapse function. The initially ingoing pulse changes its sign after imploding through the origin and becomes an outgoing pulse, as shown in the last panel evaluated at $t = 10$.

A valuable test for the GC domain decomposition algorithm is to observe an apparent horizon's formation and estimate the mass inside it. The apparent horizon forms when the expansion of outgoing null rays, Θ^+ , vanishes [30]. With the coordinate system under consideration,

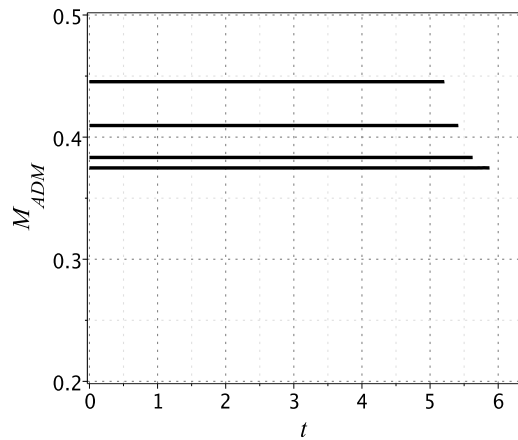


FIG. 8. ADM masses corresponding to the initial amplitudes $A_0 = 0.0082, 0.0083, 0.0086,$ and 0.009 , from bottom to top. In all cases a black hole is formed.

we have that $\Theta^+ = 0$ implies in

$$e^{-2\mu(t_{\text{AH}}, r_{\text{AH}})} \rightarrow 0, \quad (56)$$

where t_{AH} is the time of the apparent horizon formation located at r_{AH} . From the above condition, we calculate the mass at the apparent horizon directly from Eq. (8) as

$$m_{\text{AH}} = \frac{r_{\text{AH}}}{2}, \quad (57)$$

after determining r_{AH} . However, Eq. (56) implies that the metric function $\mu(t_{\text{AH}}, r_{\text{AH}}$ diverges spoiling,

as a consequence the numerical integration. In this case, we obtain r_{AH} numerically by the approximation $e^{-2\mu(t_{AH}, r_{AH})} \approx \mathcal{O}(10^{-3}) - \mathcal{O}(10^{-4})$.

We have performed simulations starting with the initial data (51) with $r_0 = 5.0$. We have previously mentioned that the apparent horizon forms if $A_0 \gtrsim 0.0082$, which represents a discrepancy with Ref. [29] that established that $A_0 \gtrsim 0.0082$. We present some ADM mass plots versus time in Fig. 8 for those solutions ending up forming an apparent horizon, which corresponds to the initial amplitudes $A_0 = 0.0082, 0.0083, 0.0086$, and 0.009 . The ADM masses remain constant until the formation of an apparent horizon when the integration breaks up. As expected, the dynamics takes a longer time for smaller initial amplitudes. We have performed the numerical simulations using a three-subdomains code with $N_\phi^{(1)} = 90$ and map parameter $L_0 = 2.0$.

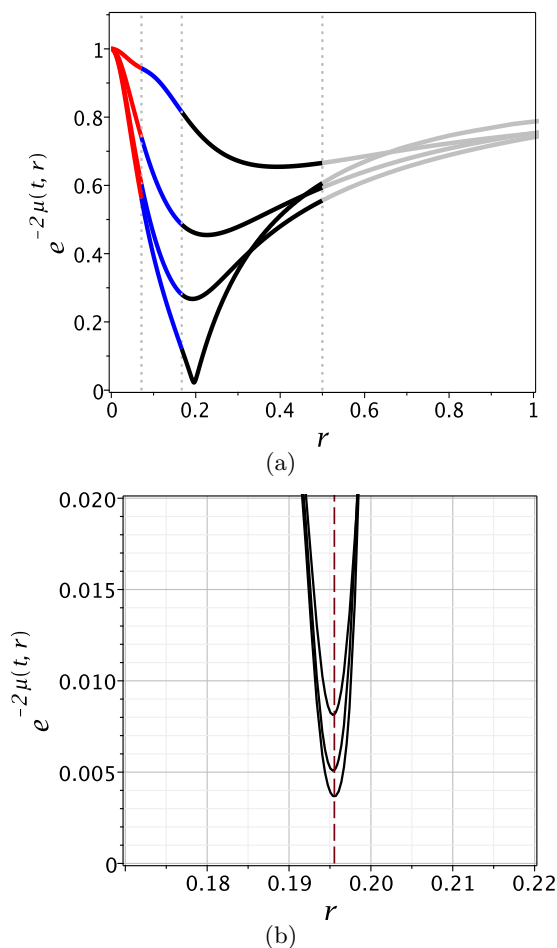


FIG. 9. (a) Plots of $e^{-2\mu(t,r)}$ showing the approach to the apparent horizon. The curves are evaluated at $\approx 2.802, 2.876, 2.892, 2.896$. (b) Fine structure of the approach to the apparent horizon prior the integration is halted. The curves are calculated at $t \approx 2.895\,632\,9, 2.895\,634\,40, 2.895\,632\,50$ from up to down

We proceed with the determination of the mass at the apparent horizon. To this aim, we have implemented a

four subdomain code and set $r_0 = 2.0$ in the initial data (51) to reduce the integration time. In this case, the numerical experiments indicated that for $A_0 \gtrsim 0.087$, an apparent horizon forms. We have also evolved the dynamical system with the adaptive Cash-Karp integrator [31]. And further, we increased the numerical resolution of the numerical scheme near the origin after placing the subdomains' interfaces at $x^{(1)} = -0.75, x^{(2)} = -0.5, x^{(3)} = 0$ in the computational auxiliary domain $-1 \leq x \leq 1$. In the physical domain, these interfaces are located at:

$$r^{(1)} = \frac{L_0}{7}, r^{(2)} = \frac{L_0}{3}, r^{(3)} = L_0.$$

Therefore, most of the collocation points are inside the region $0 \leq r \leq L_0$. Depending on the map parameter L_0 , we can concentrate the collocation points near the origin where the apparent horizon forms. For instance, considering $A_0 = 0.088$ the ADM mass is about 0.361 that corresponds to a $r_{AH} \approx 0.72$ if all mass is trapped inside the horizon, that naturally is not the case. Thus, the apparent horizon will necessarily form at $r_{AH} < 0.72$, implying that a reasonable choice would be $L_0 = 0.5$.

We present in Fig. 9 snapshots of $e^{-2\mu(t,r)}$ evaluated in several instants showing the approach to the formation of an apparent horizon. Here, the code has $N_\phi^{(1)} = 100$. We have indicated the subdomains' boundaries by dotted vertical lines, and the colors red, blue, black, and gray correspond to the first, second, third, and fourth subdomains. In Fig. 9(a), the plots from up to down are calculated at $t \approx 2.802, 2.876, 2.892, 2.896$. It becomes evident the fast approach to the apparent horizon formation. The detailed approach to the apparent horizon is shown in Fig. 9(b), where the three graphs of $e^{-2\mu(t,r)}$ located in the third subdomain approach to $r = r_{AH}$ whose minimum value is of the order of $\mathcal{O}(10^{-3})$. Notice that this minimum value takes place at $r_{AH} \simeq 0.195\,53$ that corresponds to the apparent horizon mass $M_{AH} \simeq 0.097\,8$. It is important to mention that the adaptive time step integrator was crucial to following the scalar field dynamics until the apparent horizon formed. The graphs of Fig. 9(b) correspond to $t \approx 2.895\,632\,9, 2.895\,634\,40, 2.895\,632\,50$.

In the next numerical experiments, we have considered the initial amplitudes $A_0 = 0.089, 0.090, 0.096$ and 0.10 whose corresponding ADM masses are $M_{ADM} \simeq 0.368\,458, 0.375\,726, 0.420\,091$, and $0.450\,307$, respectively. We performed the numerical simulations using a four subdomain code with better resolution, namely $N_\phi^{(1)} = 130$. Then, in Fig. 10, we present the plots of $e^{-2\mu(t,r)}$ evaluated at the end of the integration at the instants $t \approx 2.836, 2.768, 2.514, 2.407$. The location of the apparent horizon in each case is determined by the minimum of $e^{-2\mu(t,r)}$, $r = r_{AH}$ indicated by the dashed lines. In the left panels, plots correspond to $A_0 = 0.089$ and 0.090 , whereas in the right panels $A_0 = 0.095$ and 0.010 ; the apparent horizon masses are $M_{AH} \simeq 0.1153, 0.1280, 0.1864, 0.2252$. Therefore, these

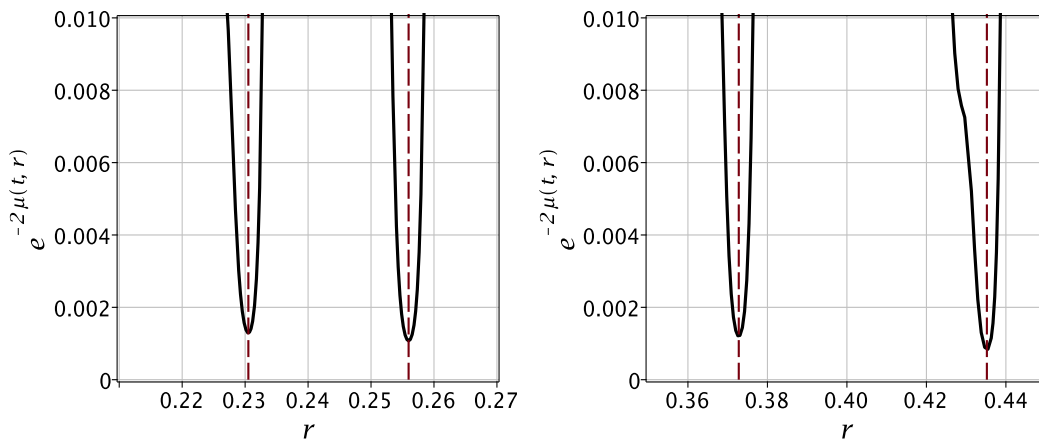


FIG. 10. Snapshots of $e^{-2\mu(t,r)}$ evaluated at the apparent horizon formation for $A_0 = 0.088, 0.089, 0.090,$ and 0.10 , from left to right. The dashed lines indicate the location of the apparent horizon radius in each case. The masses evaluated at the apparent horizon are $M_{AH} \simeq 0.1153, 0.1280, 0.1864, 0.2252$

results mean that the GC domain decomposition algorithm is effective in determining the apparent horizon masses.

V. FINAL COMMENTS

The present work is the second of a systematic development of the multidomain or domain decomposition technique connected with the Galerkin-Collocation method and applied to situations of interest in numerical relativity. In the continuity of Ref. [1], we have considered the self-gravitating and spherically symmetric scalar field in the $3+1$ formulation.

We have used the same numerical scheme of Ref. [1]: we compactified and divided the spatial domain $\mathcal{D} : 0 \leq r < \infty$ into several subdomains. An intermediate computational domain $-1 \leq x \leq 1$ is introduced using an algebraic map given by (18), and with linear mappings, we define several subdomains labeled by $-1 \leq \xi^{(l)} \leq 1$, $l = 1, 2, \dots, n$ as shown by Fig. 1. This scheme is the backbone for implementing the algorithm.

The basis functions for the scalar field, and the metric functions have a distinctive feature of satisfying the boundary conditions. In particular, the basis functions provided the exact cancellation of the $1/r$ terms near the origin, therefore eliminating a potential source of numerical errors.

We have adopted the patching method [7] for joining the subdomain solutions through the transmission conditions in the subdomains' interfaces. It represents the most straightforward version applied to a hyperbolic system since, for these categories of problems, the transmission conditions are not uniquely defined [10, 11].

We have presented numerical tests to validate the code, starting with initial data whose amplitude is close to the minimum necessary for forming an apparent horizon. We

adopted two error measures: the relative deviation of the ADM mass and the L_2 -errors associated with the Hamiltonian constraint in each subdomain. In all cases, we noticed that these error measures exhibit a spectral convergence; in other words, they decay exponentially with the increase of the truncation orders. The exponential convergence also depends on the other factors like the map parameter L_0 and the interfaces defining the subdomains size. We remind that the Hamiltonian constraint is used to determine the initial data $\mu(t_0, r)$.

It was possible to obtain the mass inside the apparent horizon by searching the minimum of $e^{-2\mu(t,r)}$ when the numerical integration diverges, which signals the formation of an apparent horizon. The introduction of multiple subdomains allowed us to concentrate more collocation points near the region where the apparent horizon forms after the scalar field hit the origin. For the case of four subdomains, with 130 collocation points in each subdomain, we have obtained $e^{-2\mu(t,r)} \sim \mathcal{O}(10^{-3})$, despite being described by an analytical function. The increase of collocation points can result in smaller levels of $e^{-2\mu(t,r)}$ at the apparent horizon.

Finally, we would point out the next steps of the present investigation. We intend to continue developing the GCDD for the dynamics in spherically symmetric spacetimes considering the field equations in the BSSN formulation [32–35] in which we can find relevant works [36–41]. For the case of a non-spherically symmetric spacetime, we are developing a GCDD algorithm for the Bondi problem [42].

ACKNOWLEDGMENTS

M. A. acknowledges the financial support of the Brazilian agency Coordenação de Aperfeiçoamento de Pessoal de Nível Superior (CAPES). W. O. B. thanks to the De-

partamento de Apoio à Produção Científica e Tecnológica (DEPESQ) for the financial support, also to the Departamento de Física Teórica for the hospitality, both at

the Universidade do Estado do Rio de Janeiro. H. P. O. thanks Conselho Nacional de Desenvolvimento Científico e Tecnológico (CNPq).

-
- [1] M. Alcoforado, W. Barreto and H. P. de Oliveira, *Multidomain Galerkin-Collocation method: characteristic spherical collapse of scalar fields*, preprint arXiv: 2009.00115.
- [2] H. P. de Oliveira and E. L. Rodrigues, *Phys. Rev. D* 90, 124027 (2014).
- [3] W. Barreto, P. C. M. Clemente and H. P. de Oliveira, *Phys. Rev. D* 97, 104035 (2018).
- [4] W. Barreto, P. C. M. Clemente, H. P. de Oliveira and B. Rodrigue-Mueller, *Gen. Rel. Grav.* 50, 71 (2018).
- [5] W. Barreto, J. A. Crespo, H. P. de Oliveira and E. L. Rodrigues, *Class. Quant. Grav.* 36, 215011 (2019).
- [6] J. A. Crespo, H. P. de Oliveira and J. Winicour, *Phys. Rev. D* 100, 104017 (2019).
- [7] C. Canuto, A. Quarteroni, M. Y. Hussaini and T. A. Zang, *Spectral Methods in Fluid Dynamics*, Springer-Verlag (1988).
- [8] C. Canuto, A. Quarteroni, M. Y. Hussaini and T. A. Zang, *Spectral Methods - Evolution to Complex Geometries and Applications to Fluid Dynamic*, Springer-Verlag (2007).
- [9] S. Orszag, *J. Comp. Phys.* 37, 70 (1980).
- [10] D. A. Kopriva, *Appl. Numer. Math.* 2, 221 (1986).
- [11] D. A. Kopriva, *SIAM J. Sci. Sta. Comp.* 10, 1 120 (1989).
- [12] E. Faccioli, F. Maggio, A. Quarteroni and A. Tagliani, *Geophysics* 61, 1160 (1996).
- [13] S. Bonazzola, E. Gourgoulhon, M. Salgado and J. A. Marck, *Astron. Astrophys.* 278, 421 (1993).
- [14] H. P. Pfeifer, *Initial data for black hole evolutions*, Ph.D. thesis (2003), arXiv:gr-qc/0510016.
- [15] M. Ansorg, *Class. Quantum Grav.* 24 S1 (2007).
- [16] Spectral Einstein Code, <https://www.black-holes.org/code/SpEC.html>
- [17] LORENE (Langage Objet pour la Relativité Numérique), <http://www.lorene.obspm.fr>
- [18] L. E. Kidder, M. A. Scheel and S. A. Teukolsky, *Phys. Rev. D* 62, 084032 (2000).
- [19] B. Szilágyi, L. Lindblom and M. A. Scheel, *Phys. Rev. D* 80, 124010 (2009).
- [20] D. A. Hemberger, M. A. Scheel, L. E. Kidder, B. Szilágyi, G. Lovelace, N. W. Taylor, S. A. Teukolsky, *Class. Quantum Grav.* 30, 115001 (2013).
- [21] M. Boyle et al., *The SXS Collaboration catalog of binary black hole simulations*, arXiv: 1904.04831 (2019).
- [22] M. Alcubierre, F. S. Guzman, T. Matos, D. Nunez, L. A. Urena-Lopez and P. Wiederhold, *Class. Quant. Grav.* 19, 5017 (2002).
- [23] M. W. Choptuik, *Phys. Rev. Letters* 70, 9 (1993).
- [24] S. L. Shapiro and S. A. Teukolsky, *The Astrophys. J.* 235, 199 (1980).
- [25] R. Arnowitt, S. Deser and C. W. Misner, *Republication of: The dynamics of general relativity*. *Gen Relativ Gravit* 40, 1997 (2008).
- [26] J. P. Boyd, *Chebyshev and Fourier Spectral Methods* (Dover Publications, New York, 2001).
- [27] R. Peyret, *Spectral methods for incompressible viscous flow*, Springer-Verlag, New York (2002).
- [28] B. Fornberg, *A practical guide to pseudospectral methods*, Cambridge University Press (1998).
- [29] M. Alcubierre, *Introduction to 3+1 numerical relativity*, Oxford University Press (2008).
- [30] T. W. Baumgarte and S. L. Shapiro, *Numerical Relativity*, Cambridge University Press (2010).
- [31] J. R. Cash and A. H. Karp, *Variable order Runge-Kutta method for initial value problems with rapidly varying righthand sides*, *ACM Transactions on Mathematical Software* 16, 201 (1990).
- [32] T. Nakamura, K. Oohara, and Y. Kojima, *Prog. Theor. Phys. Suppl.* 90, 1 (1987).
- [33] M. Shibata and T. Nakamura, *Phys. Rev. D* 52, 5428 (1995).
- [34] T. W. Baumgarte and S. L. Shapiro, *Phys. Rev. D* 59, 024007 (1999).
- [35] J. Brown, *Phys. Rev. D* 79, 104029 (2009).
- [36] A. Akbarian and M. W. Choptuik, *Phys. Rev D* 92, 084037 (2015).
- [37] E. Sorkin and M. W. Choptuik, *Gen. Rel. Grav.* 42, 1239 (2010).
- [38] M. Alcubierre, M. Corichi, J. A. Gonzales, D. Nunez, B. Reiman and M. Salgado, *Phys. Rev. D* 72, 124018 (2005).
- [39] P. J. Montero, T. W. Baumgarte, I. Cordero-Carrion and E. Mueller, *Phys. Rev. D* 87, 044026 (2013).
- [40] P. J. Montero and I. Cordero-Carrion, *J. Phys. Conf. Ser.* 454, 012002 (2013).
- [41] M. Alcubierre and M. D. Mendez, *Gen. Rel. Grav.* 43, 2769 (2011).
- [42] M. Alcoforado, W. Barreto and H. P. de Oliveira, *A spectral domain decomposition code for the Bondi problem*, in preparation.